Frequency-dependent streaming potential of Ottawa sand

Eric Tardif,[1] Paul W. J. Glover,[2] and Jean Ruel[1]

Received 21 October 2010; revised 6 January 2011; accepted 12 January 2011; published 13 April 2011.

[1] The scientific literature is almost devoid of frequency-dependent electrokinetic measurements on geological materials. An apparatus that allows the measurement of the streaming potential coupling coefficient of unconsolidated and disaggregated materials such as sands, gravels, and soils has been designed, constructed, and tested. The apparatus, which uses an electromagnetic drive, operates in the range 1 Hz to 1 kHz and has a 25.4 mm diameter sample chamber for samples up to 150 mm long. We have made streaming potential coupling coefficient measurements on samples of Ottawa sand as a function of frequency. The results have been analyzed using critically and variably damped second-order vibrational mechanics models as well as the theoretical models of Packard for capillary tubes and Pride for porous media. The best fit was provided by an underdamped second-order model with a damping factor of 0.8561 ($R^2 = 0.993$). Transition frequencies were derived from the two vibrational models and the Pride model either by fitting the model to the data or directly from the model, giving 230, 273, and 256.58 Hz, respectively. These values are in good agreement with the transition frequency expected for a sand with an independently obtained effective pore radius of 6.76×10^{-5} m from laser diffraction grain size measurements. The Packard model also agrees extremely well with the experimental data ($R^2 = 0.987$) directly providing a value of the equivalent capillary radius of 6.75×10^{-5} m that coincides within experimental errors with the independently obtained effective pore radius measurements.

Citation: Tardif, E., P. W. J. Glover, and J. Ruel (2011), Frequency-dependent streaming potential of Ottawa sand, *J. Geophys. Res.*, *116*, B04206, doi:10.1029/2010JB008053.

1. Introduction

[2] This paper examines the dependence of the streaming potential coupling coefficient on the frequency of the pressure difference across the sample that is used to generate a time-varying fluid flow and hence a time-varying streaming potential.

[3] When an ionic fluid flows in a porous medium, an electrical potential is created which is called the streaming potential [*Glover and Jackson*, 2010]. The streaming potential increases linearly with the difference in fluid pressure that drives the fluid flow, providing that the flow remains laminar [*Bolève et al.*, 2007]. The steady state streaming potential coupling coefficient is defined as the ratio of the measured streaming potential to the driving fluid pressure difference. If the fluid flow is constant, the streaming potential coupling coefficient is described by the Helmholtz-Smoluchowski equation, which was derived for capillary tubes [e.g., *Helmholtz*, 1879; *Overbeek*, 1953]. The Helmholtz-Smoluchowski equation is also used for porous and fractured rocks, but its validity has not been tested because it is not possible to measure the zeta potential of complex porous media independently. The Helmholtz-Smoluchowski equation is given by

$$C_s = \frac{\Delta V}{\Delta P} = \frac{\varepsilon \zeta}{\eta_f \sigma} \text{ where } \sigma = \sigma_f + \frac{2\Sigma_s}{\Lambda}, \quad (1)$$

where ΔP (Pa) is the fluid pressure difference, ε (F/m) is the dielectric constant of the fluid, η_f (Pa s) is the dynamic viscosity of the fluid, ζ(V) is the zeta potential, ΔV(V) is the streaming potential, σ_f (S/m) is the electrical conductivity of the bulk fluid, Σ_s (S) is the specific electrical conductance of the surface (i.e., that due to the double layer), σ (S/m) is the electrical conductivity of the mobile fluid, and Λ (m) is a characteristic length associated with the microstructure of the pore network. The steady state streaming potential is independent of the sample geometry.

[4] Recently several modified versions of the classical HS equation have been published that take account of the variability of the streaming potential coupling coefficient as a function of grain size [*Revil et al.*, 1999; *Glover and Déry*, 2010], pore size [*Glover and Déry*, 2010] and pore throat size [*Glover and Déry*, 2010].

[5] There are a number of models that can be applied to frequency dependent streaming potentials in rocks. The first two models examine the system as an ideal vibrational system of the second order with critical and variable

[1]Department of Mechanical Engineering, Université Laval, Quebec, Quebec, Canada.
[2]Department of Geology and Engineering Geology, Université Laval, Quebec, Quebec, Canada.

0148-0227/11/2010JB008053

damping. This type of model is standard in engineering and is well described by *Thomson and Dahleh* [1998].

[6] The amplitude of the critically damped second-order vibrational behavior is given by

$$C_s(\omega) = \frac{C_{so}}{\sqrt{\left(1 + \left(\frac{\omega}{\omega_t}\right)^2\right)}}, \tag{2}$$

where $C_s(\omega)$ (in V/MPa) is the streaming potential coupling coefficient at a frequency ω (in Hz), C_{so} (in V/MPa) is the steady state streaming potential coupling coefficient and ω_t (in Hz) is the transition frequency. This model only exists in the real domain.

[7] The amplitude of the ideal second-order behavior with variable damping is given by

$$C_s(\omega) = \frac{C_{so}}{\sqrt{\left(1 - \left[\frac{\omega}{\omega_t}\right]^2\right)^2 + \left(2\left[\frac{\omega}{\omega_t}\right]\zeta_d\right)^2}}, \tag{3}$$

where ζ_d is the damping factor of the system. This equation provides the modulus or magnitude of the vibration as is usually measured experimentally either by using a peak-to-peak or an RMS measurement. Here RMS is the usual root mean square value as commonly used in statistics and electrical engineering. However, it can be written in terms of its real and imaginary components as

$$\Re(C_s(\omega)) = \frac{C_{so}\left(1 - [\omega/\omega_t]^2\right)}{\left(1 - [\omega/\omega_t]^2\right)^2 + (2\zeta_d\omega/\omega_t)^2}, \tag{4}$$

$$\Im(C_s(\omega)) = \frac{-C_{so}(2\xi\omega/\omega_t)}{\left(1 - [\omega/\omega_t]^2\right)^2 + (2\zeta_d\omega/\omega_t)^2}. \tag{5}$$

Each of these components can be calculated from the measured amplitude and phase angle.

[8] While these two models are generic in that they can be applied to any forced harmonic oscillating system, there are also models which are specific to porous media. The first of these is due to *Packard* [1953]. Packard's model is based on the Navier-Stokes equation and was formulated for capillary tubes. The Packard model can be written

$$C_s(\omega) = \left(\frac{\varepsilon\,\zeta}{\eta_f\,\sigma}\right)\left(\frac{2}{kr}\,\frac{J_1(kr)}{J_0(kr)}\right), \tag{6}$$

where

$$k = \sqrt{\frac{-i\omega\rho_f}{\eta_f}}$$

and $i = \sqrt{-1}$, ρ_f(kg/m^3) is the density of the bulk fluid, ω(rad/s) is the angular frequency, r (m) is the radius of the capillary tube in which the flow takes place and J_0 and J_1 are Bessel functions of the zeroth and first order, respectively. Note that k has dimensions of inverse length; hence kr is dimensionless. The real part of the Bessel function expression $\Re(2\,J_1(kr)/kr\,J_0(kr))$ varies between unity at low frequencies and zero at high frequencies, and its imaginary part $\Im(2\,J_1(kr)/kr\,J_0(kr))$ is zero at both low and high frequencies but attains a peak value at a frequency known as the transition frequency [*Walker and Glover*, 2010].

[9] The *Packard* [1953] model has recently been simplified by *Reppert et al.* [2001], who provide an approximation derived from equation (6) that is also only formally valid for capillary tubes.

$$C_s(\omega) = \left(\frac{\varepsilon\,\zeta}{\eta_f\,\sigma}\right)\left(1 - \frac{2}{r}\sqrt{\frac{\eta_f}{\omega\,\rho_f}}\left[\frac{1}{\sqrt{2}} - i\frac{1}{\sqrt{2}}\right]\right). \tag{7}$$

In section 6.2 we show that the validity range of this model is severely limited by an assumption that was made in its derivation.

[10] By contrast, the equation of *Pride* [1994] was derived from first principles for porous media and takes the form

$$C_s(\omega) = \left(\frac{\varepsilon\,\zeta}{\eta_f\,\sigma}\left(1 - 2\frac{\delta}{\Lambda}\right)\right) \cdot \left(1 - i\frac{\omega}{\omega_t}\frac{m^*}{4}\left[1 - 2\frac{\delta}{\Lambda}\right]^2\left[1 - i^{\frac{3}{2}}\delta\sqrt{\frac{\omega\,\rho_f}{\eta_f}}\right]^2\right)^{-\frac{1}{2}} \tag{8}$$

where

$$\omega_t \equiv \frac{\phi}{\tau_e\,\kappa_{DC}}\,\frac{\eta_f}{\rho_f} \tag{9}$$

$$m^* \equiv \frac{\phi\,\Lambda^2}{\tau_e\,\kappa_{DC}} \tag{10}$$

[11] In equation (8) τ_e (unitless) is the electrical tortuosity of the pore network, ϕ (unitless) is the porosity of the sample, κ_{DC} (m^2) is the steady state fluid permeability, and δ (m) is the Debye length. The parameter ω_t (rad/s) is the transition frequency, at which the quadrature component of the dispersive system is greatest, and which is important to characterize the frequency dependency of the streaming potential coupling coefficient and to predict the DC fluid permeability. Finally, a simplification of the equation (8) has recently been proposed [*Walker and Glover*, 2010] using techniques that were developed to transform effective grain radii and effective pore radii [*Glover and Walker*, 2009] and assuming that the Debye length is always negligible compared to the characteristic pore size

$$C_s(\omega) = \left(\frac{\varepsilon\,\zeta}{\eta_f\,\sigma}\right)\left(1 - 2\,i\left[\frac{\Lambda}{r_{eff}}\right]^2\frac{\omega}{\omega_t}\right)^{-1/2}, \tag{11}$$

where

$$\omega_t = \frac{\phi}{\tau_e\,\kappa_{DC}}\,\frac{\eta_f}{\rho_f} = \frac{8}{r_{eff}^2}\,\frac{\eta_f}{\rho_f}. \tag{12}$$

In equations (11) and (12), r_{eff} (m) is the effective pore radius of the rock, and the transition frequency is in rad/s. Equation (12) is valid for all porous media. *Reppert et al.* [2001] reached the same equation in their work for capil-

Table 1. Physical Properties of Ottawa Sand

Property	Unit	Measured (This Work)	*Gorman and Kelly* [1990]	Comment
Modal grain radius (Laser diffraction), r_g	μm	251 ± 56	-	Using a Malvern Mastersizer 2000.
Modal grain radius (Image analysis), r_g	μm	245 ± 46	-	Image analysis using Sigma Scan 4
Modal grain radius (Hg injection), r_g	μm	211 ± 59	-	Calculated from pressure data using Mayer-Stowe theory
D10 grain radius (Sieving), r_g	μm	-	130	
Effective pore radius, r_p	μm	67.6 ± 16.2	-	Using the method of *Glover and Walker* [2009]
Effective pore throat radius, r_{pt}	μm	40.7 ± 9.0	-	Using *Glover and Déry* [2010], for random packing.
Modal pore throat radius (Hg injection), r_{pt}	μm	38.5 ± 7.5	-	Using a Micromeritics Autopore IV
Porosity (Gravimetry)	-	0.314	0.36–0.42	Please see text.
Porosity (Helium expansion)	-	0.325	-	Using a real gas expansion pycnometer.
Porosity (Mercury injection)	-	0.304	-	Using a Micromeritics Autopore IV
Permeability, κ	m^2	1.19×10^{-10}	0.366×10^{-10}[a]	The measured permeability is the mean over many cycles.
Electrical conductivity, σ_r	S/m	0.2301	0.1914[a]	For a 0.1 mol/L NaCl at 25°C with $\sigma_f = 1.07593$ S/m.
Formation factor, F	-	4.676	5.62[a]	*Gorman and Kelly* [1990] value interpolated from their data
Connectedness, G	-	0.214	0.178[a]	Calculated from the formation factor [*Glover*, 2009]
Cementation exponent, m	-	1.372	1.536[a]	Calculated from the formation factor [*Glover*, 2009]
Theta factor, Θ	-	3.705	-	From the method of *Glover and Walker* [2009]
Predicted transition frequency, ω_t	Hz	273	-	At 24°C using the method of *Walker and Glover* [2010]

[a]The formation factor has been calculated by interpolating the measured He porosity in the $F(\phi)$ data of *Gorman and Kelly* [1990] ($F = 10.5$–15ϕ) then using it to calculate G, m and σ_r using standard equations. *Gorman and Kelly* [1990] measured the hydraulic conductivity K, which we have converted to permeability using $\kappa = K\eta_f/\rho_f g$, where $\eta_f = 8.94 \times 10^{-4}$ Pa s, $\rho_f = 997$ kg/m^3 and $g = 9.81$ m/s.

lary tubes (their equation 33), which is a good indication of the concordance between the *Packard* [1953], *Reppert et al.* [2001], *Pride* [1994], and *Walker and Glover* [2010] models. *Reppert et al.* [2001] also showed that their approximation for capillary tubes (equation (7)) is consistent with the Pride model (equation (8)) providing that parameters describing capillary tubes are taken (i.e., $m = 8$, $\phi = 1$, $\tau_e = 1$, $\Lambda = r$, $\kappa_{DC} = r^2/8$).

[12] These models seem to be self-consistent. However, they should be treated with care since none of them can be said to be supported by experimental data. There is very little experimental data available for the frequency-dependent streaming potential of porous media. Those which are available (5 sizes of capillary tube, 2 filters, 1 glass membrane and 1 rock) were gathered together in a comprehensive review by *Walker and Glover* [2010] and shown to fit equation (12) well. It is extremely clear that there is a great need for high-quality frequency-dependent streaming potential coupling coefficient data on earth materials. Here we begin by describing such measurements for Ottawa sand, and analyze the resulting data with the models described above.

2. Sample Material

[13] Ottawa sand (Fisher Scientific) was used for all the measurements. Its main properties are shown in Table 1. Samples of the Ottawa sand were washed repeatedly in distilled water in order to remove any rock powder. They were then dried in a vacuum oven prior to use. The results shown in this paper were carried out on one sand pack that was constructed by filling the tube successively with 1 cm thick layers of sand that were tamped down. It is likely that there will be a natural variability in the results between different sand packs made with the same raw material. This paper does not address this variation.

[14] The pore throat and grain size distributions of the sample material were measured using mercury injection porosimetry, and are shown in Figure 1 together with the grain size distribution obtained by laser diffraction measurements using a Malvern Mastersizer 2000. The porosity of sand samples was also measured using a real gas expansion porosimetry using helium, which has been developed within our laboratory. The electrical properties of a sample of the sand was made using a Solartron 1260A Impedance Analyzer. The electrical and microstructural properties of the sand used in this work were found to agree very well with those obtained by *Gorman and Kelly* [1990] as shown in Table 1. The only slight difference is that in the measured grain diameter (502 μm for our work and 260 μm for the "density" grade Ottawa sand used by *Gorman and Kelly* [1990]). However, the porosity, formation factor and cementation exponents seem to agree very well. Assuming the sand grains to be perfectly spherical, one would expect the formation factor, porosity, cementation exponent and electrical conductivity all to be dependent on the grain size. One possible explanation for the apparent discrepancy is that the values quoted by Gorman and Kelly are really their grain radii. If this were so, all the data from both works would be consistent.

[15] The absolute value of the complex electrical conductivity at the frequency for which the out-of-phase conductivity was minimum has been used together with the modal grain size from the laser diffraction measurements and the helium porosity in order to calculate the mean pore size of the sand samples using the method of *Glover and Walker* [2009].

[16] The fluid used in the experiments was 0.001 mol/L NaCl with a measured density of 997 kg/m^3, which agrees well with the equation of state of NaCl solutions [e.g., *Lvov and Wood*, 1990] and a viscosity of 8.94×10^{-4} Pa s calculated using the model of *Phillips et al.* [1978]. The quasi-steady state permeability was obtained by calculating the volume of fluid flowing through the sample per second at 10 Hz using the measured piston displacement and also measuring the pressure required to move this fluid. The permeability at 10 Hz was $\kappa_{10} = 1.19 \times 10^{-10}$ m^2. We have

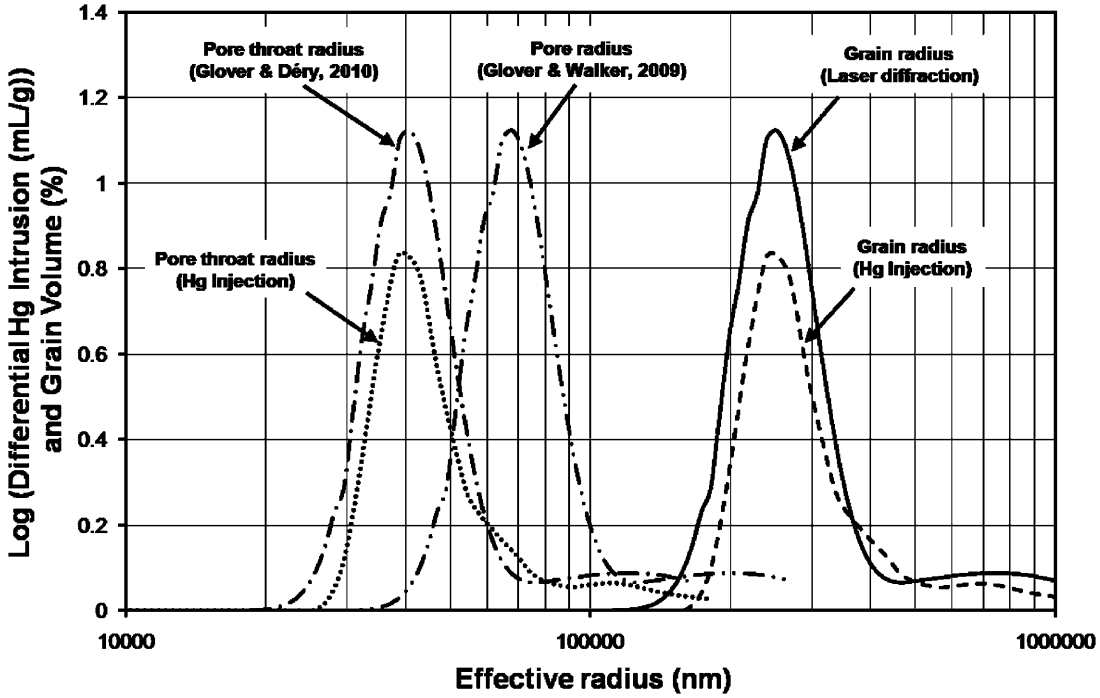

Figure 1. Grain diameter, pore diameter, and pore throat diameter spectra for Ottawa sandstone. Solid line, grain radius by laser diffraction; dash double dotted line, pore radius by theta transformation; dash single dotted line, pore throat radius calculated from the pore radius; dotted line, pore throat radius by mercury injection porosimetry; short dashed line, grain size diameter by mercury injection porosimetry.

taken this value to represent the steady state permeability in the absence of steady state permeability on the sample. It should be noted that our measurement of κ_{10} is larger than that obtained by *Gorman and Kelly* [1990] for Ottawa sand. They actually measured the hydraulic conductivity K of their samples, obtaining $K = [4 \pm 1] \times 10^{-4}$ m/s for their 'density sand' when packed to give a porosity of about 0.325, which is equivalent to $\kappa_{DC} = [0.366 \pm 0.091] \times 10^{-10}$ m^2 when converted to permeability. In the absence of specific data from *Gorman and Kelly* [1990] we have used $T = 25$°C, $\eta_f = 0.84 \times 10^{-4}$ Pa s, $\rho_f = 997$ kg/m^3 and $g = 9.81$ m/s^2 to make the conversion. This is a reasonable step as they used slightly saline Nebraska tap water as their fluid at room temperature. The sand that *Gorman and Kelly* [1990] used had a mean grain diameter of 2.60×10^{-4} m compared to $[5.02 \pm 1.12] \times 10^{-4}$ m and $[4.22 \pm 1.18] \times 10^{-4}$ m for our sand depending on whether the laser diffraction data or the mercury injection data is used, respectively. If we invoke the RGPZ model of permeability in rocks [*Glover et al.*, 2006] we can see that $\kappa \propto d^2$. Hence, we would expect our sample to have a permeability between 2.63 and 3.72 times that of the Gorman and Kelly values, i.e., between $[0.962 \pm 0.508] \times 10^{-10}$ m^2 and $[1.362 \pm 0.642] \times 10^{-10}$ m^2 which is the case.

3. Experimental Apparatus

[17] The measurements were made using an instrument that was designed and built by ourselves for the purpose of making frequency-dependent streaming potential measurements on unconsolidated and disaggregated earth materials. Figure 2 shows diagrams and an image of the apparatus. The heart of the apparatus is a thick tube of polycarbonate (Figure 2b, label 1) which is a good electrical insulator, resists corrosion well, and is mechanically strong and transparent. We consider that it is important to be able to inspect the sample (Figure 2b, label 2) to ensure that no air bubbles or cavitation are present during operation. The sample is held between two polycarbonate disks (Figure 2b, label 3) each of which has holes drilled in it to allow the unimpeded passage of fluid. The disks allow the unimpeded passage of fluid, but not the grains. For finer grained samples we add two layers of fine mesh, one oriented at 45° to the other, on the inside of the disks. The disks are held in

Figure 2. (a) Diagram of the apparatus for making frequency-dependent streaming potential measurement on nonconsolidated materials: 1, sample tube; 2, sand sample; 3, polycarbonate disk; 4, spring; 5, output endcap; 6, piston endcap; 7, piston; 8, one-way valve (fluid in); 9, fluid out; 10, Ag/AgCl electrodes; 11, dynamic pressure transducers; 12, 13, 16, 17, rigid frame and vibration-damped feet; 14, LVDT; 15, dynamic shaker. (b) Close-up of the sample tube with connections: 1, Perspex sample tube; 2, Ottawa sand sample; 3, drilled Perspex sample support; 4, stainless steel circlip; 5, stainless steel spring; 6 and 7, aluminum screwed endcaps 8, streaming potential electrodes; 9, electrode access ports; 10, dynamic pressure transducers; 11, piston. (c) Image of the working apparatus with Faraday cage and signal processing boards.

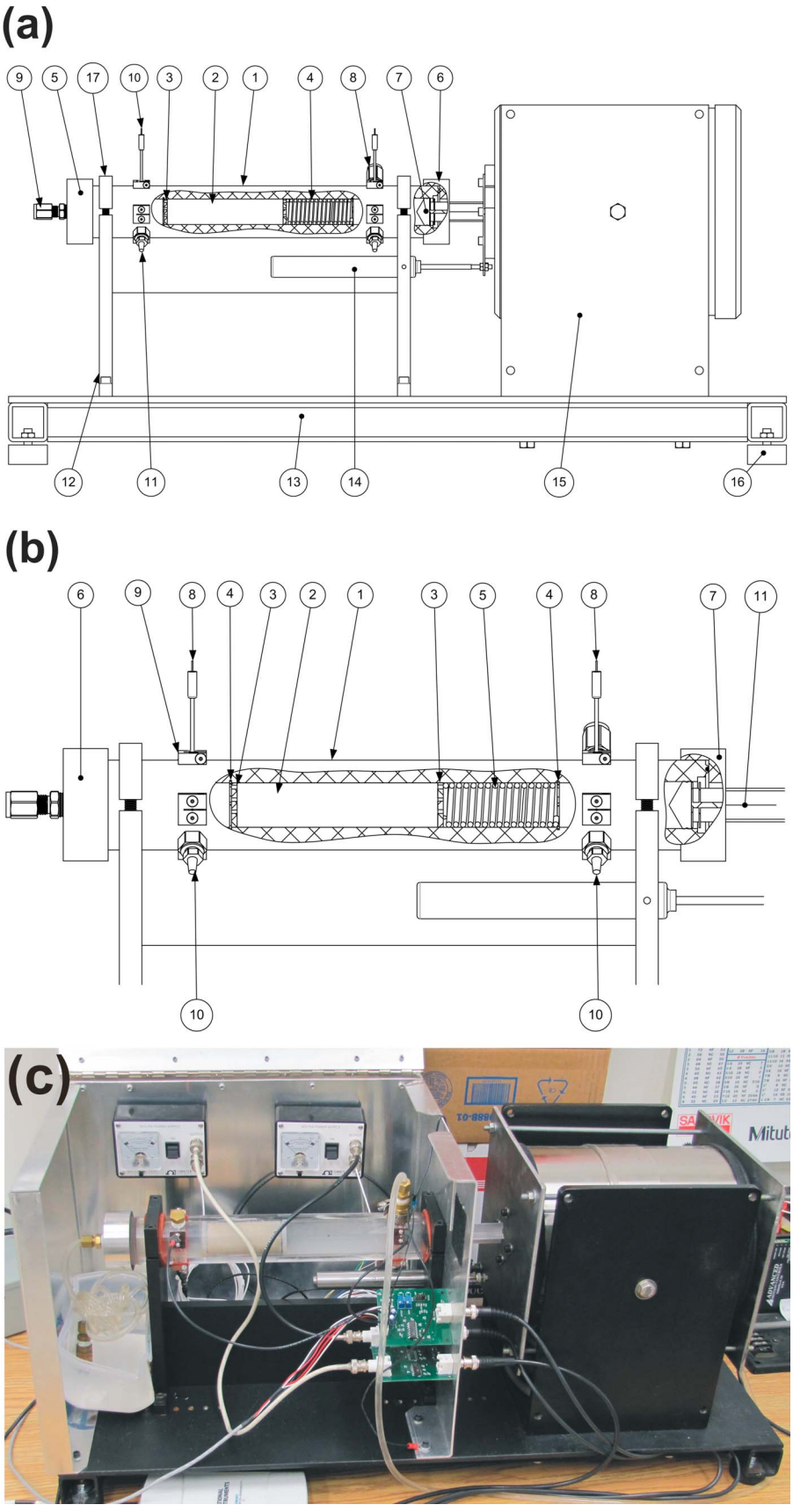

Figure 2

place by two stainless steel circlips (Figure 2b, label 4). The sample is held in a compact form using a spring (Figure 2b, label 5) on the upstream side of the sample to ensure that its dynamic properties have no effect on the frequency-dependent properties of the sample. There are four ports at each end of the sample tube, which are arranged radially (with a 90° spacing). Two at each end are tapped with a 1/4 inch NPT tapered thread. One of these ports at each end is used for dynamic pressure transducers (Figure 2b, label 10). The other tapered port at the piston end of the tube is fitted with a nonreturn valve which allows fluid to enter the sample tube, while the remaining port at the fluid output end of the sample tube remained unused and sealed in this work. There are also two 2 mm diameter holes at each end of the sample tube that are directly opposite the tapered ports. These are fitted with a compressed "O"-ring seal (Figure 2b, label 9) which allows the insertion of nonpolarizing electrodes (Figure 2b, label 8). Each end of the tube is terminated by an aluminum cap. That at the output end (Figure 2b, label 6) contains a connector for water to leave the cell, while that at the piston end (Figure 2b, label 7) contains a hole for the piston (Figure 2b, label 11).

[18] There are only three items in the flow path that are made from stainless steel (two circlips (Figure 2b, label 4) and a spring (Figure 2b, label 5)). Since these items are completely immersed in the flow path and are completely isolated from an external earth, any redox potentials that may be associated with them do not affect the measured streaming potential.

[19] The electrodes are Ag/AgCl nonpolarizing electrodes from Cypress Systems (66-EE009). They consist of a PEEK tube that is 2 mm in diameter and 4 cm long, the end of which is sealed with a porous ceramic. The pressure transducers are DPX101–250 dynamic transducers from Omega, with a resonant frequency of 500 kHz, a low-frequency limit of 0.08 Hz and a maximum frequency of 170 kHz, and which each use an ultrastable ACC-PS1 power supply. It was found that the streaming potential coupling coefficient measurements had an unacceptably high level of power line electrical noise, 29 dB with respect to the signal. The noise was attenuated by 46 dB using a Faraday cage, and custom designed preamplification, making it −17 dB with respect to the signal before cycle averaging. Signal averaging was used to remove the small amounts of line noise that remained, resulting in a final noise level that is −51 dB with respect to the signal. Both pressure transducers can be seen in Figure 2c. The apparatus was also fitted with a linear variable differential transducer (LVDT) from Omega (LD610–15) in order to measure the position of the piston to within 1.5 μm. All transducers were logged using a National Instruments USB-6211 data logger with a LabView user interface. Analysis of the streaming potential and the differential pressure measurement shows the absolute accuracy to be better than ±3% and ±2%, respectively.

[20] The piston is driven by a VTS100 electromagnetic shaker from Dynamic Solutions that uses a permanent magnet (Figure 2a, label 15). This shaker is capable of a maximum force of 445 N and a peak-to-peak displacement of 2 cm. The critical characteristic of shakers based on permanent magnets is that they have extremely good force to acceleration ratios (0.302 Ns^2/m for the VTS100), which allows them to provide large forces that can be varied extremely quickly. The VTS-100 a frequency range from 2 to 6.5 kHz, which is more than sufficient for our requirements. The shaker was driven by a AMC 20A14 high power DC amplifier and triggered using an GW Instek SFG-2110 signal generator providing a sine wave, which together allow control of both the frequency and the peak-to-peak piston displacement. It is extremely important that the shaker, LVDT and the sample tube are held rigidly. A steel support frame was constructed to provide this (Figure 2a, labels 12, 13, 16, and 17).

4. Experimental Methodology

[21] Experiments were carried out in the following way. The tube was packed with a sample of Ottawa sand. Since the tube was of a known uniform diameter and transparent, it was possible to use (1) the difference in the weights of the empty and packed tube, (2) the density of the sand, and (3) the length of the sand column in order to calculate the mean porosity of the sample. Once the sample was packed in the sample tube with the spring and end caps in place, the sample was saturated with the process fluid through the piston bore by holding the tube vertically until all air bubbles had been evacuated. The piston was added and the tube was returned to the horizontal and put in the rigid frame. The transducers and fluid connections were then fitted, followed by the associated signal processing boards. Fluid was pumped through the sample under a back pressure in order to expel the final air bubbles. The fluid circulation also allowed the sand to equilibrate with the fluid, avoiding electrochemical and electrothermal potentials.

[22] The apparatus may be used in several modes: (1) steady state flow using a pump to flow fluid into port 8 and out of port 9 of Figure 2a, (2) frequency-dependent flow imposed by the piston alone with no net flow, (3) frequency-dependent flow imposed by the piston with flow entering the sample tube via a one-way valve placed at port 8 of Figure 2a, and (4) frequency-dependent flow imposed by the piston with a DC flow imposed by an external pump. All the results in this paper were made using the third method.

[23] One source of significant electrical noise is the electromagnetic shaker itself. We carried out electrical potential measurements at 20 frequencies between 1 Hz and 1 kHz and found that the RMS noise caused by the shaker was 20 μV at 1 Hz, less than 40 μV in the frequency range 1 to 100 Hz, and less than 58 μV between 100 and 1 kHz. We hypothesized that the source of the noise was probably a slight mechanical vibration that was transmitted from the shaker to the sample through the frame. In order to reduce the noise level associated with mechanical vibration, an additional mass of 40 kg was added to the frame. This addition reduced the high-frequency noise by −6.48 dB. These tests show clearly how important it is to have a rigid framework, but also confirm that the noise in the present apparatus is negligible (−51 dB) compared with the signal.

[24] Another concern was that the displacement of the piston might have an influence on the measured streaming potential. Twenty two measurements of the streaming potential coupling coefficient were made as a function of RMS piston displacement during augmentation of the amplitude from 1 to 22 mm and then while it was reduced to

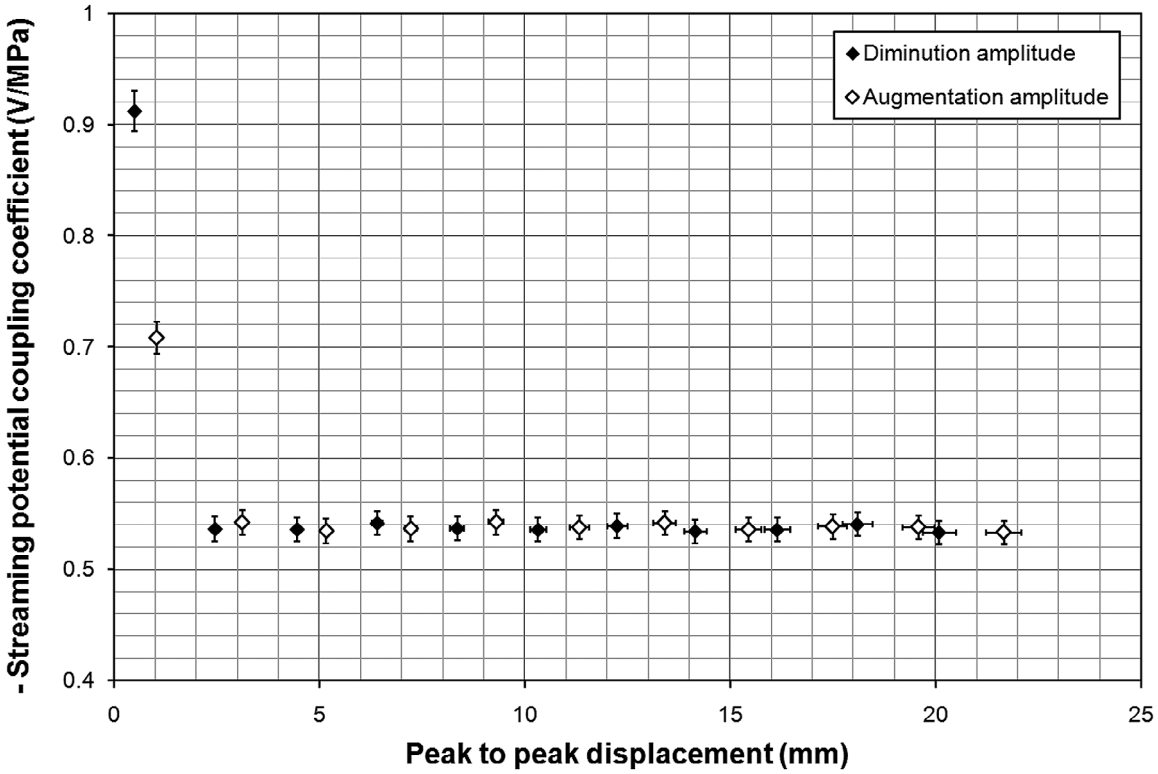

Figure 3. Streaming potential coupling coefficient measured at 10 Hz as a function of piston displacement while increasing the piston displacement (solid symbols) and then reducing the piston displacement (open symbols).

0.5 mm. The results, which are shown as a function of peak to peak displacement in Figure 3, indicate clearly that there is no effect of piston displacement on the measured streaming potential coupling coefficient except for peak to peak displacements less than about 2 mm. At these small displacements, the developed pressure is very small (<50 μV) and it is difficult to differentiate the streaming potential that has been generated from the background noise.

[25] The results shown in this work were made on a sample which was 25 mm in diameter and 80 mm long and which was fully saturated with 0.001 mol/L NaCl in chemical and thermal equilibrium with the sample. The density and viscosity of the process fluid were 997 kg/m^3 and 8.94×10^{-4} Pa s, respectively. The measurements were made at a temperature of 24.0 ± 0.8°C. The size of the errors in frequency were calculated from the half width of the principal peak in the Fourier transform of the streaming potential. The size of the errors in the streaming potential coupling coefficient were calculated from the standard deviation/standard error in the mean of data representing 100 cycles.

5. Experimental Results

[26] Figure 4 shows typical data from a streaming potential coupling coefficient measurement on Ottawa sandstone at 20 Hz. In Figure 4a, the black dotted line shows the displacement of the piston to be sinusoidal. The fluid pressure difference that results from the piston movement is quasi-sinusoidal as shown by the dashed line. The small excursions from true sinusoidal behavior may be due to nonlinear behavior in the mechanical system or may be due to the effects of piston friction. The streaming potential that is generated is shown as the solid line. It is important to note that the streaming potential is in antiphase with the applied fluid pressure, as required by theory, and that it exactly mirrors the fluid pressure curves. This indicates that the

Figure 4. (a) Typical measurements of normalized piston position (dotted line), fluid pressure difference (dashed line), and generated streaming potential (solid line) as a function of time during the passage of 0.001 mol/L NaCl through a sample of fully saturated Ottawa sand at a frequency of 20 Hz and a temperature of 24.0 ± 0.8°C. (b) Fourier transform of the measured streaming potential data sampled in Figure 4a as a function of frequency. (c) The measured streaming potential as a function of the measured fluid pressure difference for 10 cycles of a typical measurement at 20 Hz. The curves superimpose themselves to produce a thick line for both the forward and return cycles of the driving piston that shows hysteresis. These curves can be seen individually in the magnified insert top right.

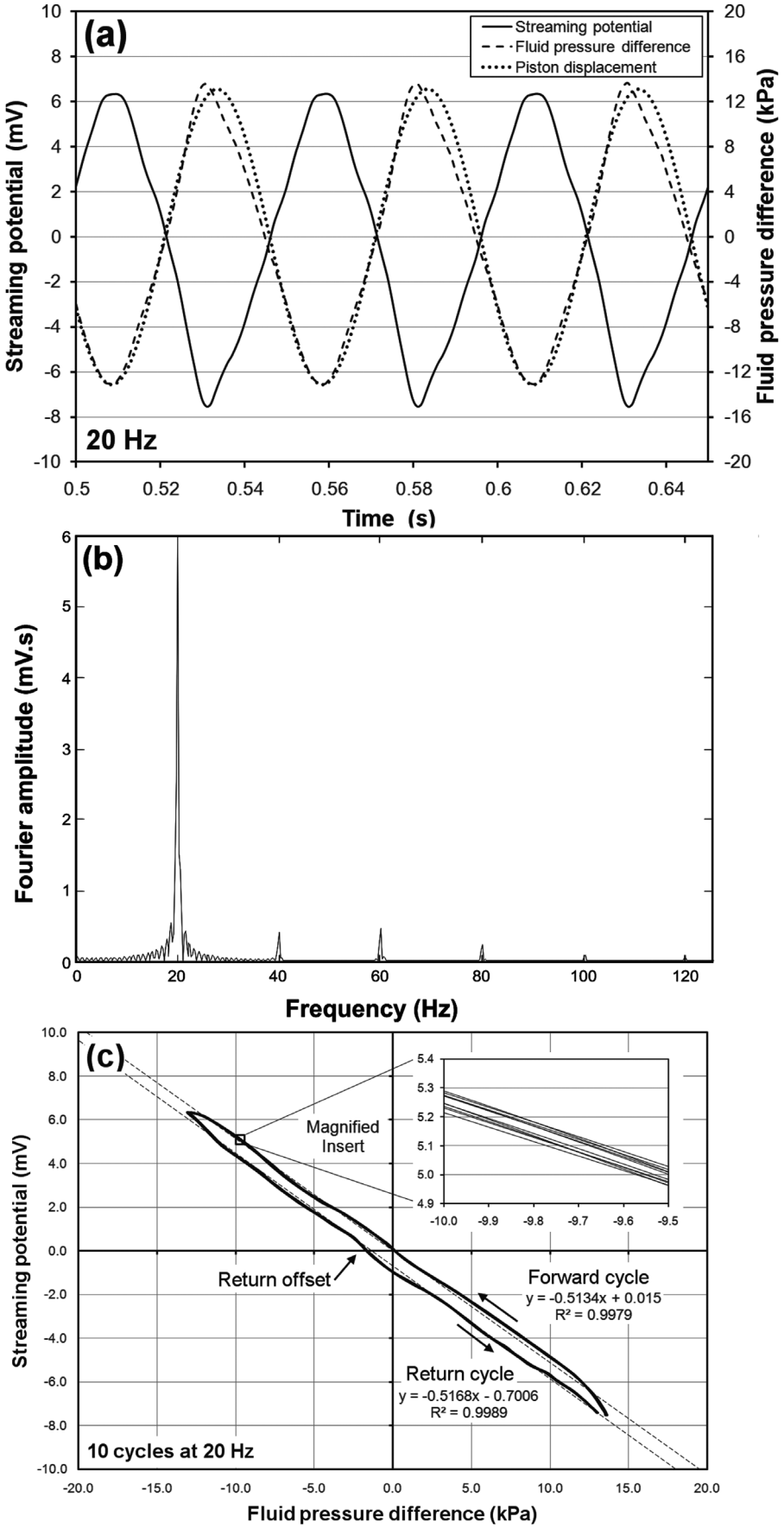
(a)
Streaming potential
Fluid pressure difference
Piston displacement
Streaming potential (mV)
Fluid pressure difference (kPa)
20 Hz
Time (s)
(b)
Fourier amplitude (mV.s)
Frequency (Hz)
(c)
Magnified Insert
Streaming potential (mV)
Return offset
Forward cycle
y = -0.5134x + 0.015
R² = 0.9979
Return cycle
y = -0.5168x - 0.7006
R² = 0.9989
10 cycles at 20 Hz
Fluid pressure difference (kPa)

Figure 4

coupling between the applied fluid pressure and the generated streaming potential is approximately linear, which concurs with theoretical requirements. Figure 4c, a plot of the streaming potential as a function of the driving fluid pressure difference, shows there to be a slight hysteresis between the forward and return cycles. Please note that the gap in the hysteresis at the bottom right of Figure 4c is an artifact of the data processing. The magnified insert shows the variability between 10 consecutive cycles to be of the order of ±50 μV, which concurs with our previous analysis of the errors involved in the measurement. The forward cycle conforms to a straight line passing very close to the origin ($\Delta V = -0.5134 \times \Delta P + 0.015$ mV) with $R^2 = 0.9979$, and the return cycle also conforming to a straight line but with a phase lag ($\Delta V = -0.05168 \times \Delta P - 0.7006$ mV) with $R^2 = 0.9989$. While the forward cycle clearly provides the higher quality data, it is interesting to note that both the forward and return cycle are highly linear and provide a slope that is almost the same. This indicates that the use of the return cycle data or the combined use of both will not have a significant impact on the final measured streaming potential coupling coefficient.

[27] We have carried out a Fourier transform of the streaming potential data and the results are shown in Figure 4b. The frequency spectrum is dominated by the signal frequency (20 Hz) and there are harmonics at 20 Hz multiples that diminish with frequency. Although the 60 Hz harmonic is slightly larger than one would expect it to be, due to remaining unsuppressed line frequency noise, it is remarkable that line frequency noise is suppressed so well in the apparatus. The lack of noise indicates the reliability of the measurement. Similar tests have been carried out for other frequencies and provide similar results.

[28] Figure 5 shows the streaming potential coupling coefficient of samples of Ottawa sandstone in the range 1 to 1 kHz.

[29] The streaming potential coupling coefficient in the low-frequency limit C_{so}, which is represented in our data by the point at 5 Hz ($C_s(\omega = 5) = 0.518$ V/MPa). Physical modeling of the zeta potential and the streaming potential coupling coefficient of the Ottawa sand using the approach of *Glover and Déry* [2010] gives values of $\zeta = -15.9$ mV and $C_{so} = 1.04$ V/MPa for $\Gamma_o = 5$ sites/nm^2, $F = 4.67$, $m = 1.37$, $r_{grain} = 2.51 \times 10^{-4}$ m, $pH = 6$, $pK_{me} = 7.5$, $pK\text{-} = 8$. The measured value for the streaming potential coupling coefficient is consistent with the data compilation for silica-based earth materials made by *Jaafar* [2009] and subsequently used by *Jaafar et al.* [2009] and *Vinogradov et al.* [2010], as can be seen in Figure 6.

6. Theoretical Modeling

[30] We have fitted six models to the experimental data; two that examine the system as an ideal vibrational system of the second order, the model of *Packard* [1953] for capillary tubes and its simplification by *Reppert et al.* [2001], and the model of *Pride* [1994] with the simplification made under the thin double layer assumption by *Walker and Glover* [2010].

6.1. Vibrational Mechanics Models

[31] The critically damped second-order vibrational behavior is given by equation (2) and is shown in Figure 5a. It is clear that this model fits the data reasonably well ($R^2 = 0.973$) but has a shallower roll-off than the experimental data. The transition frequency provided by fitting the model to the data is $\omega_t = 230$ Hz.

[32] The variably damped second-order vibrational behavior is given by equation (3), and is also shown in Figure 5a. Qualitatively, this fits the data much better, with a reiterative fitting giving $R^2 = 0.993$, and providing $\omega_t = 273$ Hz and $\zeta_d = 0.8561$. The streaming potential coupling coefficient in Ottawa sandstone follows the classical vibrational theory for a harmonically driven forced oscillating system.

6.2. Capillary Tube Models

[33] Figure 5b shows the results of fitting the *Packard* [1953] model to the data. This model was derived for capillary tubes. Hence it might be expected not to fit the data perfectly. However, contrary to expectations the *Packard* [1953] fitted the data very well with $R^2 = 0.987$. Since the fluid density and viscosity are known and fixed, the only variable parameter in this model is the radius of the capillary tube, r. We found $r = 6.75 \times 10^{-5}$ m for the *Packard* [1953] model, which is almost exactly the same as that obtained from the laser diffraction measurements.

[34] We have attempted to fit the *Reppert et al.* [2001] version of the *Packard* [1953] model to our data with no success. We believe the lack of success is due to a problem with the model that we briefly describe below. The *Reppert et al.* [2001] model is given by equation (7). This equation can be very simply separated into its real and imaginary parts.

$$\begin{aligned} \Re(C_s(\omega)) &= \left(\frac{\varepsilon\zeta}{\eta_f\sigma}\right)\left(1 - \frac{2}{r}\sqrt{\frac{\eta_f}{2\omega\rho_f}}\right) \\ \Im(C_s(\omega)) &= \left(\frac{\varepsilon\zeta}{\eta_f\sigma}\right)\left(\frac{2i}{r}\sqrt{\frac{\eta_f}{2\omega\rho_f}}\right) \end{aligned} . \qquad (13)$$

[35] It is immediately clear that both the real and imaginary parts of the streaming potential coupling coefficient are proportional to $\omega^{-1/2}$. Such a variation cannot match the form of the data in Figure 5 no matter what values of the other parameters are taken. The problem lies in the derivation of equation (7). *Reppert et al.* [2001] derived their

Figure 5. Normalized streaming potential coupling coefficient of Ottawa sand saturated with 0.001 mol/L NaCl at a temperature of 24.0 ± 0.8°C as a function of frequency (a) compared with the critically damped and underdamped second-order vibrational mechanics models given by *Thomson and Dahleh* [1998], for $\omega_t = 230$ and 273 Hz, respectively, and (b) compared with the models of *Packard* [1953] for an equivalent capillary radius $r_{eff} = 1.65 \times 10^{-4}$ m, and (c) the model of *Pride* [1994] and the approximation of that model by *Walker and Glover* [2010], for $\omega_t = 256.58$ Hz.

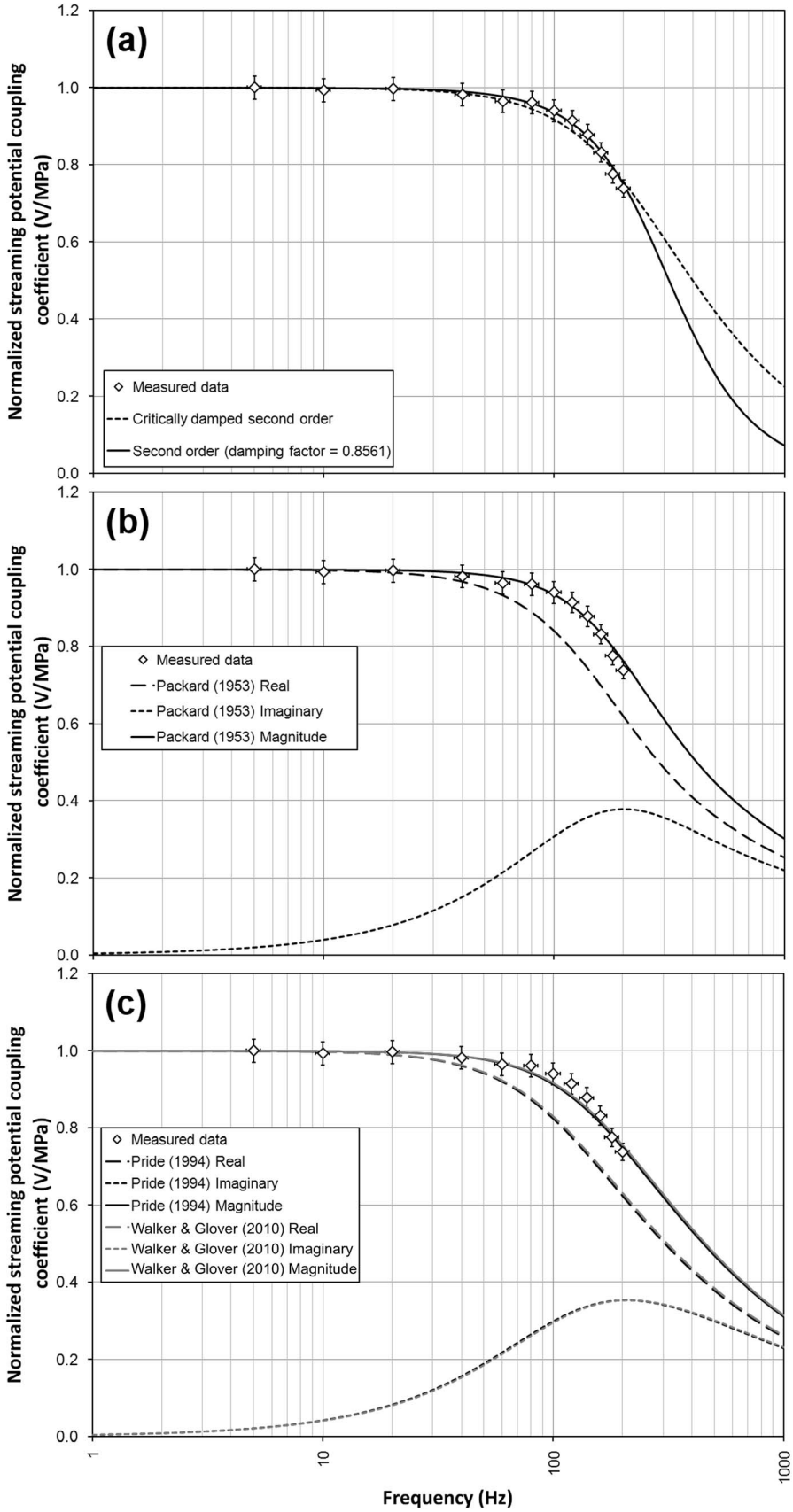
(a)
Normalized streaming potential coupling coefficient (V/MPa)
Measured data
Critically damped second order
Second order (damping factor = 0.8561)
(b)
Normalized streaming potential coupling coefficient (V/MPa)
Measured data
Packard (1953) Real
Packard (1953) Imaginary
Packard (1953) Magnitude
(c)
Normalized streaming potential coupling coefficient (V/MPa)
Measured data
Pride (1994) Real
Pride (1994) Imaginary
Pride (1994) Magnitude
Walker & Glover (2010) Real
Walker & Glover (2010) Imaginary
Walker & Glover (2010) Magnitude
0.0
0.2
0.4
0.6
0.8
1.0
1.2
1
10
100
1000
Frequency (Hz)

Figure 5

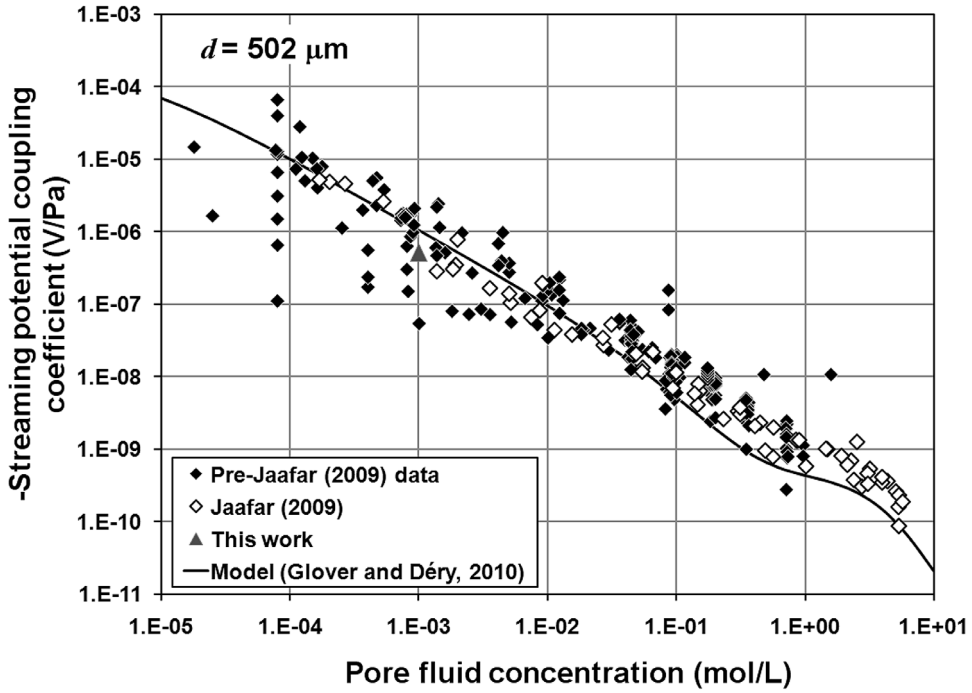

Figure 6. The steady state streaming potential coupling coefficient measured in this work (gray triangle) shown with a compilation of silica-based earth materials measured by (open symbols) or compiled by (solid symbols) [*Jaafar*, 2009]. The line represents the theoretically modeled streaming potential coupling coefficient using the method of *Glover and Déry* [2010] with the parameters Γ_o = 5 sites/nm^2, F = 4.67, m = 1.37, r_{grain} = 2.51 × 10^{-4} m, pH = 6, pK_{me} = 7.5, pK- = 8, and T = 24.0°C.

model from the *Packard* [1953] model by using the "high-frequency approximation" that

$$\frac{J_1\left(x\sqrt{-i}\right)}{J_0\left(x\sqrt{-i}\right)} = -i, \tag{14}$$

for which they cite *Crandall* [1926] and *Abramowitz and Stegun* [1964]. This is a mathematical approximation that is generally true providing the x value in the equation is sufficiently large. The value of x will take different values for different physical problems. In our case [*Reppert et al.*, 2001, equation (23)]

$$x = r\sqrt{\rho_f \omega/\eta_f}. \tag{15}$$

Hence, we must examine the left hand side of equation (14) to ascertain the value of x above which the equation may be taken to be valid, then use this value with equation (15) to calculate the value of frequency above which the derivation of *Reppert et al.* [2001] will also be valid.

[36] Figure 7 shows the behavior of the real and imaginary parts of the left hand side of equation (14) as a function of both x and frequency. There are two x axes. One shows the x value, and represents the mathematically general case. The other shows the frequency, which has been calculated from the x value using equation (15) and ρ_f = 997 kg/m^3, η_f = 8.94 × 10^{-4} Pa s, and r = 6.76 × 10^{-5} m, which are the parameters that best represent our experimental conditions and will be approximately the same as other experimental determinations on real rocks using aqueous fluids. For x < 10 (ω < 3120 Hz) equation (14) gives real values which are significantly different from zero, while the imaginary component rapidly tends to zero as x and the frequency decrease. It is clear that the approximation given in equation (14) is not valid in this range. For x = 10 (ω = 3120 Hz) equation (14) gives a value of 0.0367–0.9648i, which is not sufficiently near 0–i for the approximation given by equation (14) to be considered valid. For x = 100 (ω = 0.31 MHz) equation (14) gives a value of 0.0035–0.9965i, which is now near enough to 0–i for the approximation given by equation (14) to be considered valid. Hence we can say, that for rocks with a pore size in the order of tens of microns that are saturated with aqueous pore fluids at ambient temperatures, equation (14), and by extension the *Reppert et al.* [2001] model is only truly valid for frequencies above about 0.3 MHz.

6.3. Porous Media Models

[37] Finally, we have implemented the model of *Pride* [1994] in its exact form and in the simplified form given by *Walker and Glover* [2010]. The *Pride* [1994] model was produced by considering the low-frequency and high-frequency behaviors of the streaming potential coupling coefficient and combining them. These models have two advantages over the models that have been described previously. The first is that it was conceived specifically for porous media. The second is that there are no unknown variables in the models if one has a full set of electrical and hydraulic parameters for the porous medium, as in our case.

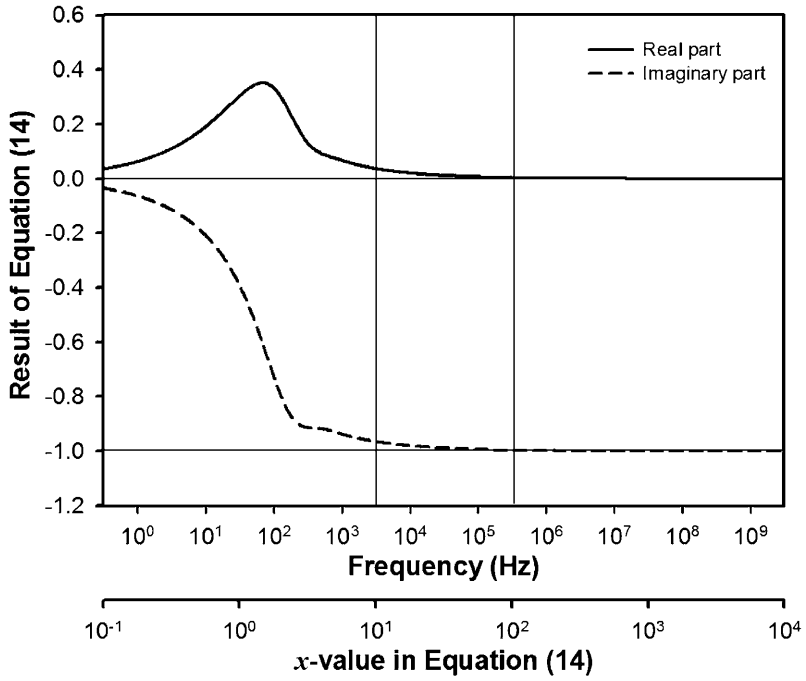

Figure 7. The value of equation (14) as a function of the x variable and as a function of the frequency. The frequency axis has been constructed using the x value in equation (15) with $\rho_f = 997$ kg/m^3, $\eta_f = 8.94 \times 10^{-4}$ Pa s, and $r = 6.76 \times 10^{-5}$ m, which are the parameters that best represent our experimental conditions and which will be approximately the same as other experimental determinations on real rocks using aqueous fluids.

Figure 5c shows the results of fitting both models to the data. For the Pride model we used a characteristic pore scale length $\Lambda = 3.9 \times 10^{-5}$ m, which was calculated from the pore radius using equation (20) of *Walker and Glover* [2010], and a Debye length $\delta = 9.6 \times 10^{-9}$ m which was calculated from the pore fluid salinity at 24°C in the standard way [e.g., *Revil and Glover*, 1997]. Since $\delta \ll \Lambda$ we have $2\delta/\Lambda \ll 1$ in equation (8), and it is possible to say that the thin electrical double layer assumption is justified. Hence, we would expect that the simplification to the *Pride* [1994] model by *Walker and Glover* [2010] to also be valid. Equation (10) allows us to calculate the value of $m^* = 2.73$ using $\phi = 0.325$, $\Lambda = 3.9 \times 10^{-5}$ m, the electrical tortuosity $\tau_e = \phi^{(1-m)} = 1.519$, and the measured steady state permeability $\kappa_{DC} = 1.19 \times 10^{-10}$ m^2. This value of m^* is close to the theoretical value of $m^* = 8/3 = 2.6\dot{6}$ obtained by *Walker and Glover* [2010]. The transition frequency is not a fitting variable, rather it is obtained directly from equation (9) using independent measurements of porosity, electrical tortuosity and hydraulic permeability already discussed as well as the density and viscosity of the pore fluid, which is also well known. We have carried out both procedures and have obtained $\omega_t = 256.58$ Hz with $R^2 = 0.967$.

[38] The simplified version of the *Pride* [1994] model by *Walker and Glover* [2010] that is given in equation (11) has also been fitted to the data and gives results which are almost indistinguishable from those from the full Pride implementation because $\delta \ll \Lambda$. The transition frequency is the same as that in the full Pride implementation by definition (i.e., $\omega_t = 256.58$ Hz). In fact the *Walker and Glover* [2010] modification of the Pride model fits the data slightly better than the full implementation ($R^2 = 0.969$) which is probably due to measurement errors in the parameters that it contains. It is interesting to note that equation (11) can be simplified further using the results from *Glover and Walker* [2009] and *Walker and Glover* [2010] to give

$$\left(\frac{\Lambda}{r_{eff}}\right)^2 = \frac{1}{3}, \tag{16}$$

which leads to equation (11) becoming independent of the characteristic pore scale Λ and the effective pore size r_{eff} so that the microstructural control on the frequency-dependent streaming potential coupling coefficient is expressed entirely through the transition frequency in the form of equation (12). Equation (11) then becomes

$$C_s(\omega) = \left(\frac{\varepsilon\,\zeta}{\eta_f\,\sigma}\right)\left(1 - i\frac{2}{3}\frac{\omega}{\omega_t}\right)^{-1/2}. \tag{17}$$

Figure 8. The electrokinetic transition frequency as a function of the inverse square characteristic pore size (a) in full and (b) at expanded scale to show the new data. The dashed lines represent the theoretical result [*Walker and Glover*, 2010] at four different temperatures. The data points for Ottawa sandstone were measured at 24.0°C ± 0.8°C and are shown in the context of existing experimental data for capillary tubes, filters frits, and rocks [*Walker and Glover*, 2010, Figure 6].

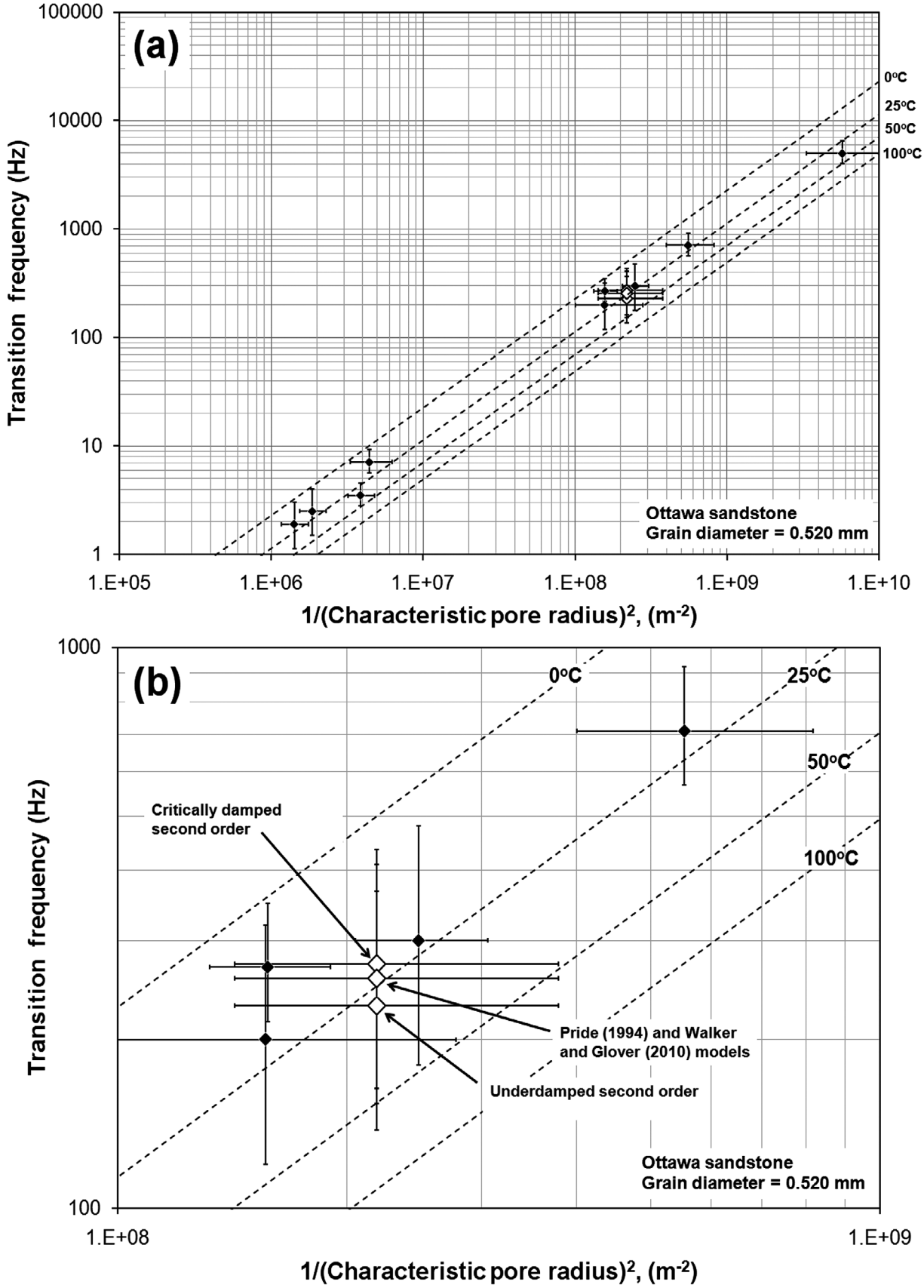
(a)
Transition frequency (Hz)
100000
10000
1000
100
10
1
0°C
25°C
50°C
100°C
Ottawa sandstone
Grain diameter = 0.520 mm
1.E+05
1.E+06
1.E+07
1.E+08
1.E+09
1.E+10
1/(Characteristic pore radius)², (m⁻²)
(b)
Transition frequency (Hz)
1000
100
0°C
25°C
50°C
100°C
Critically damped
second order
Pride (1994) and Walker
and Glover (2010) models
Underdamped second order
Ottawa sandstone
Grain diameter = 0.520 mm
1.E+08
1.E+09
1/(Characteristic pore radius)², (m⁻²)

Figure 8

[39] Both the full implementation of the *Pride* [1994] model and its simplification by *Walker and Glover* [2010] show a shallower roll-off than the measured data. This is because they are both modified forms of the critically damped second-order vibrational behavior. This type of behavior may not be optimal for the streaming potential coupling coefficient. We recommend that physical models that follow an underdamped second-order vibrational behavior are examined with the goal of finding a physical model that fits the data even better.

6.4. Transition Frequency and Pore Radius

[40] Equation (12) is derived from the *Pride* [1994] theory and indicates that the transition frequency is related to the effective pore radius of the porous medium. This relationship was tested recently for all the then available data by *Walker and Glover* [2010]. The data available to them amounted to 5 sizes of capillary tube, 2 filters, 1 glass membrane and 1 rock. They found that all the data was consistent with equation (12) at a temperature of about 25°C. Here we repeat the figure used by *Walker and Glover* [2010] including the three new data points (Figure 8). These are based on the transition frequencies for the data on Ottawa sand that are presented in this work that have been derived from the critically and underdamped ($\zeta_d = 0.8561$) second-order vibrational models and the *Pride* [1994] model (which is identical to that of the *Walker and Glover* [2010] simplification). It is clear that the transition frequencies obtained from the data and models fit very well with the independently obtained pore radius measurements.

[41] The transition frequencies for the critically damped and underdamped vibrational mechanics models and the *Pride* [1994] model (230, 273, and 256.58 Hz, respectively) can be substituted directly into equation (12) to provide characteristic pore radii, which are $[7.04 \pm 0.282] \times 10^{-5}$ m, $[6.47 \pm 0.258] \times 10^{-5}$ m, and $[6.67 \pm 0.266] \times 10^{-5}$ m, respectively. These values compare extremely well with the value of $[6.76 \pm 0.162] \times 10^{-5}$ m obtained from applying the theta transformation [*Glover and Walker*, 2009] to the laser diffraction grain size measurements. We note that if these transition frequencies are used to predict the steady state permeability of the sand we get $[1.33 \pm 0.05] \times 10^{-10}$ m^2, $[1.12 \pm 0.04] \times 10^{-10}$ m^2, and $[1.19 \pm 0.05] \times 10^{-10}$ m^2, respectively, which agree extremely well with the measured value $\kappa_{DC} = [1.19 \pm 0.06] \times 10^{-10}$ m^2 (120.58 ± 6.1 D).

7. Conclusions

[42] An apparatus for the measurement of the frequency-dependent streaming potential coupling coefficient of non-consolidated and disaggregated materials has been designed, constructed and tested. It has been designed to allow measurements from 1 Hz to 1 kHz to be carried out on samples that are packed into a 25.4 mm diameter tube and between 50 and 150 mm in length. Initial experiments that have been carried out on Ottawa sand indicate that the dispersive processes predicted by various theoretical model exist in Ottawa sand.

[43] We have examined the data using six model of three different types. The first type is a generic second-order vibrational model, which we have used with critical damping and with variable damping. The second type is the physical model of *Packard* [1953] that was conceived for flow through capillary tubes, and its simplification by *Reppert et al.* [2001]. The third type is a physical model provided by *Pride* [1994] that was created for porous media, and its simplification by *Walker and Glover* [2010]. We found major problems in the derivation of the Reppert *et al.* model which we believe makes it invalid for use is geological porous media. Of the other models, the best fit was provided by the underdamped second-order vibrational model with a damping factor of 0.8561 ($R^2 = 0.993$). The critically damped second-order vibrational model, the physical model of Pride and its simplification by Walker and Glover all fitted the data reasonably well ($R^2 = 0.973$, 0.967, and 0.969, respectively), but all showed a shallower roll-off at high frequencies than the measured data. Examination of the physical models shows them to be modifications of a critically damped system. It is therefore recommended that new physical models are developed containing noncritical damping terms to account for the experimental data. The Packard capillary tube model fitted the data extremely well ($R^2 = 0.987$) directly providing a value for the equivalent capillary radius of 6.75×10^{-5} m.

[44] Transition frequencies were derived from the two vibrational models and the *Pride* [1994] model either by fitting the model to the data or directly from the model, giving 230, 273, and 256.58 Hz, respectively. These values are in good agreement with the transition frequency expected for a sand with an independently measured effective pore radius of 6.76×10^{-5} m, which represents a validation of the Pride model and its *Walker and Glover* [2010] simplification.

[45] We regard this work to be a promising beginning to measurements of frequency-dependent electrokinetic properties of porous media. It is clear that the transition frequency is measureable, can be modeled using a number of approaches, and is linked to the microstructure of the porous medium. Hence, it may be possible to use frequency-dependent electrokinetic measurements to provide more information about the microstructure of the porous medium. There is also the potential for using this approach to predict both frequency-dependent and steady state permeability.

[46] **Acknowledgments.** This work has been made possible thanks to funding by the Natural Sciences and Engineering Research Council of Canada Discovery Grants Program. We would also like to thank Guillaume Lalande and Emilie Walker for their help and the members if the mechanical engineering workshop for their technical help and attention to detail.

References

Abramowitz, M., and I. A. Stegun (1964), *Handbook of Mathematical Functions With Formulas, Graphs, and Mathematical Tables*, 1046 pp., U. S. Natl. Bur. of Stand., Washington, D. C.

Bolève, A., A. Crespy, A. Revil, F. Janod, and J. L. Mattiuzzo (2007), Streaming potentials of granular media: Influence of the Dukhin and Reynolds numbers, *J. Geophys. Res.*, *112*, B08204, doi:10.1029/2006JB004673.

Crandall, I. B. (1926), *Theory of Vibrating Systems and Sound*, 272 pp., D. Van Nostrand, New York.

Glover, P. W. J., and N. Déry (2010), Streaming potential coupling coefficient of quartz glass bead packs: Dependence on grain diameter, pore size, and pore throat radius, *Geophysics*, *75*(6), F225, doi:10.1190/1.3509465.

Glover, P. W. J., and M. Jackson (2010), Borehole electrokinetics, *Leading Edge*, *29*, 724–728, doi:10.1190/1.3447786.

Glover, P. W. J., and E. Walker (2009), Grain-size to effective pore-size transformation derived from electrokinetic theory, *Geophysics*, *74*(1), E17–E29, doi:10.1190/1.3033217.

Glover, P. W. J., I. I. Zadjali, and K. A. Frew (2006), Permeability prediction from MICP and NMR data using an electrokinetic approach, *Geophysics*, *71*(4), F49–F60, doi:10.1190/1.2216930.

Gorman, T., and W. E. Kelly (1990), Electrical-hydraulic properties of unsaturated Ottawa sands, *J. Hydrol.*, *118*, 1–18, doi:10.1016/0022-1694(90)90247-U.

Helmholtz, H. (1879), Studieren über electrische Grenzschichten, *Ann. Phys. Chem.*, *7*, 337–382.

Jaafar, M. Z. (2009), Measurement of streaming potential for oilfield monitoring in intelligent wells, Ph.D. thesis, Imp. Coll. London, London.

Jaafar, M. Z., J. Vinogradov, and M. D. Jackson (2009), Measurement of streaming potential coupling coefficient in sandstones saturated with high salinity NaCl brine, *Geophys. Res. Lett.*, *36*, L21306, doi:10.1029/2009GL040549.

Lvov, S. N., and R. H. Wood (1990), Equation of state of aqueous NaCl solutions over a wide range of temperatures, pressures and concentrations, *Fluid Phase Equilib.*, *60*, 273–287, doi:10.1016/0378-3812(90)85057-H.

Overbeek, J. T. G. (1953), Thermodynamics of electrokinetic phenomena, *J. Colloid Sci.*, *8*, 420–427, doi:10.1016/0095-8522(53)90026-9.

Packard, R. G. (1953), Streaming potentials across glass capillaries for sinusoidal pressure, *J. Chem. Phys.*, *21*, 303–307, doi:10.1063/1.1698876.

Phillips, S. L., H. Ozbek, and R. J. Otto (1978), Basic energy properties of electrolytic solutions database, paper presented at Sixth International CODATA Conference, CODATA Secr., Santa Flavia, Italy, 22–25 May.

Pride, S. (1994), Governing equations for the coupled electromagnetics and acoustics of porous media, *Phys. Rev. B*, *50*, 15,678–15,696, doi:10.1103/PhysRevB.50.15678.

Reppert, P. M., F. D. Morgan, D. P. Lesmes, and L. Jouniaux (2001), Frequency-dependent streaming potentials, *J. Colloid Interface Sci.*, *234*, 194–203, doi:10.1006/jcis.2000.7294.

Revil, A., and P. W. J. Glover (1997), Theory of ionic-surface electrical conduction in porous media, *Phys. Rev. B*, *55*, 1757–1773, doi:10.1103/PhysRevB.55.1757.

Revil, A., P. A. Pezard, and P. W. J. Glover (1999), Streaming potential in porous media: 1. Theory of the zeta potential, *J. Geophys. Res.*, *104*(B9), 20,021–20,031, doi:10.1029/1999JB900089.

Thomson, W. T., and M. D. Dahleh (1998), *Theory of Vibration With Applications*, 5th ed., 524 pp., Prentice-Hall, Englewood Cliffs, N. J.

Vinogradov, J., M. Z. Jaafar, and M. D. Jackson (2010), Measurement of streaming potential coupling coefficient in sandstones saturated with natural and artificial brines at high salinity, *J. Geophys. Res.*, *115*, B12204, doi:10.1029/2010JB007593.

Walker, E., and P. W. J. Glover (2010), Permeability models of porous media: Characteristic length scales, scaling constants and time-dependent electrokinetic coupling, *Geophysics*, *75*(6), E235, doi:10.1190/1.3506561.

P. W. J. Glover, Department of Geology and Engineering Geology, Université Laval, Sainte-Foy, Québec, QC G1V 0A6, Canada. (paglover@ggl.ulaval.ca)

J. Ruel and E. Tardif, Department of Mechanical Engineering, Université Laval, Pavillon Pouliot, 1026 av. de la Médecine, Québec, QC G1V 0A6, Canada.